Oxalate-curcumin–based probe for micro- and macroimaging of reactive oxygen species in Alzheimer's disease

Jian Yang[a,b,1], Xueli Zhang[a,b,1], Peng Yuan[c,d,1], Jing Yang[a,e], Yungen Xu[b], Jaime Grutzendler[c], Yihan Shao[f], Anna Moore[a], and Chongzhao Ran[a,2]

[a]Molecular Imaging Laboratory, Athinoula A. Martinos Center for Biomedical Imaging, Massachusetts General Hospital and Harvard Medical School, Boston, MA 02129; [b]School of Pharmacy, China Pharmaceutical University, Nanjing 210009, China; [c]Department of Neurology, Yale University, New Haven, CT 06520; [d]Department of Biology, Stanford University, Stanford, CA 94304; [e]School of Pharmaceutical Sciences, Soochow University, Suzhou 215006, China; and [f]Department of Chemistry and Biochemistry, University of Oklahoma, Norman, OK 73019

Edited by Gregory A. Petsko, Weill Cornell Medical College, New York, NY, and approved October 6, 2017 (received for review April 14, 2017)

Alzheimer's disease (AD) is an irreversible neurodegenerative disorder that has a progression that is closely associated with oxidative stress. It has long been speculated that the reactive oxygen species (ROS) level in AD brains is much higher than that in healthy brains. However, evidence from living beings is scarce. Inspired by the "chemistry of glow stick," we designed a near-IR fluorescence (NIRF) imaging probe, termed CRANAD-61, for sensing ROS to provide evidence at micro- and macrolevels. In CRANAD-61, an oxalate moiety was utilized to react with ROS and to consequentially produce wavelength shifting. Our in vitro data showed that CRANAD-61 was highly sensitive and rapidly responsive to various ROS. On reacting with ROS, its excitation and emission wavelengths significantly shifted to short wavelengths, and this shifting could be harnessed for dual-color two-photon imaging and transformative NIRF imaging. In this report, we showed that CRANAD-61 could be used to identify "active" amyloid beta (Aβ) plaques and cerebral amyloid angiopathy (CAA) surrounded by high ROS levels with two-photon imaging (microlevel) and to provide relative total ROS concentrations in AD brains via whole-brain NIRF imaging (macrolevel). Lastly, we showed that age-related increases in ROS levels in AD brains could be monitored with our NIRF imaging method. We believe that our imaging with CRANAD-61 could provide evidence of ROS at micro- and macrolevels and could be used for monitoring ROS changes under various AD pathological conditions and during drug treatment.

Alzheimer's disease | reactive oxygen species | oxalate | curcumin | fluorescence imaging

Alzheimer's disease (AD) is a terminal neurodegenerative disease with no cure. The prevalent drug development strategies, which are largely predicated on amyloid and tau hypotheses, have not been successful in delivering effective treatment (1, 2). This strongly indicates that other factors, such as reactive oxygen species (ROS), should also be taken into account in AD drug development. AD is closely associated with oxidative stress, and it has long been speculated that, in AD brains, the ROS levels are significantly higher than in the healthy brains (3, 4). However, evidence from living beings for this speculation is rare (5).

At the microlevel, amyloid beta (Aβ) plaques and neurofibrillary tau tangles are the most pronounced and characteristic hallmarks of AD (1). In the past decades, the toxicity degree of Aβ plaques has been heavily disputed (1, 6, 7). Several postmortem studies suggest that the plaque abundance correlates poorly with the severity of AD (8, 9). However, preclinical studies in cell and animal models strongly assert that plaques still play important roles in AD pathogenesis (10–13). Numerous studies suggest that Aβ plaques are not static, but rather, they grow and expand dynamically throughout AD progression. Hyman and coworkers (11, 12) show that newly formed plaques can alter the curvature of neurites and spine density. Bacskai and coworkers (13) show that the plaques inhibit mitochondrial function and calcium homeostasis, which leads to rapid cell death in the vicinity of the plaques because of oxidative stress. Grutzendler and coworkers (10) show that plaques grow gradually over months, with slower growth in older AD mice, and the degree of neuritic dystrophy correlates with the speed and extent of plaque enlargement. Remarkably, new plaques induce a disproportionately large area of neuritic dystrophy. These results suggest that Aβ plaques can be categorized into "active" and "inactive/silent" plaques, and this categorization could potentially provide more rational explanations for the poor correlations between Aβ plaque loading and the severity of AD (8, 9). It is likely that active plaques could serve as important biomarkers at the early/presymptomatic stages of AD and could be a plausible therapeutic target for drug development. However, imaging methods for differentiating active and inactive plaques are currently absent.

The birth of Aβ plaques is caused by high local concentrations of Aβ peptides (11), which accumulate as soluble Aβs oligomers and insoluble fibrils. The growth of the newly born plaques is sustained by incoming soluble Aβs, which are attracted to the site and are further aggregated/cross-linked to expand the plaques (10, 14). During the formation and growth of the plaques, numerous ROS are generated; particularly, ROS are produced through Fenton reaction of Aβs with metal ions during Aβ cross-linking (15). The generated ROS can induce an overaccumulation of

Significance

It has long been speculated that Alzheimer's disease (AD) is tightly associated with oxidative stress and high concentrations of reactive oxygen species (ROS) in the brain. However, comprehensive evidence from living beings is rare. In this report, inspired by the "chemistry of glow stick," we designed oxalate-curcumin–based imaging probes to provide evidence of high ROS concentrations in AD brains in animal studies at micro- and macrolevels. At the microlevel, our imaging method identified "active" amyloid beta plaques and cerebral amyloid angiopathy via dual-color two-photon imaging. At the macrolevel, our probe could detect relatively high ROS concentrations in AD brains using near-IR fluorescence imaging. We believe that our method will be an indispensable tool for investigating ROS in living beings.

Author contributions: Jian Yang, X.Z., P.Y., and C.R. designed research; Jian Yang, X.Z., P.Y., Jing Yang, Y.S., and C.R. performed research; Jian Yang, X.Z., P.Y., and C.R. contributed new reagents/analytic tools; Jian Yang, X.Z., P.Y., Y.S., and C.R. analyzed data; and Jian Yang, X.Z., P.Y., Jing Yang, Y.X., J.G., Y.S., A.M., and C.R. wrote the paper.

The authors declare no conflict of interest.

This article is a PNAS Direct Submission.

[1]Jian Yang, X.Z., and P.Y. contributed equally to this work.

[2]To whom correspondence should be addressed. Email: cran@nmr.mgh.harvard.edu.

This article contains supporting information online at www.pnas.org/lookup/suppl/doi:10.1073/pnas.1706248114/-/DCSupplemental.

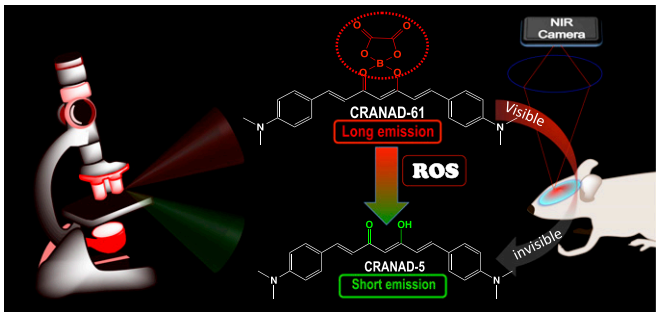

Fig. 1. Our design strategy for ROS-sensitive imaging probes. The designed probe CRANAD-61, on reaction with ROS, produces a significant Em wavelength shift, which can be used for identifying active plaques and CAAs via dual-color two-photon microscopic imaging. The shifting can also lead to a visible to invisible transformation in an NIR window (640–900 nm), as CRANAD-5, the product of the ROS reaction, is invisible with an NIR camera. This transformation could be harnessed for a whole-brain NIRF imaging to quantify the total relative ROS concentrations in AD brains.

inflammatory cytokines, such as TNFα (16), which can further attract microglia to encircle the plaques (14, 16, 17). The surrounding microglia release more ROS and contribute to the neuronal loss (17). Based on the above facts, it is plausible that active plaques are surrounded by high concentrations of ROS, which can be considered as a signature feature of active plaques, and utilized to differentiate active plaques from inactive plaques.

At the macrolevel, the speculated high ROS levels in AD brains are resulting not only from active plaques but also, from other factors, such as forming of Aβs oligomers and tau tangles, neuroinflammation, microglia activation, and overaccumulation of metal ions (15, 18). Although numerous methods have been reported for ROS imaging of cells and peripheral targets (19–34), in vivo imaging methods for ROS detection in brains, including AD brains, are still lacking. In addition, imaging probes that can be used for imaging ROS at both micro- and macrolevels are in shortage as well.

In this report, inspired by the "chemistry of glow stick," we designed and validated that CRANAD-61, an oxalate-curcumin–based near-IR fluorescence (NIRF) probe, could be used for imaging ROS at both micro- and macrolevels in vivo via wavelength shifting (Fig. 1). We first showed that, via dual-color two-photon imaging, the spectral shifting of CRANAD-61 could be used to identify active plaques and cerebral amyloid angiopathies (CAAs) that are surrounded by high ROS concentrations and that the ratiometric (long-/short-wavelength) readout could be used for mapping the heterogeneity of the ROS concentration around an Aβ plaque. In addition, we showed via whole-brain NIRF imaging that CRANAD-61 could be used for reporting relative ROS concentrations in AD brains and for monitoring changes in ROS levels with aging in AD mouse brains.

Results

Design of the Imaging Probe CRANAD-61. Our probe design strategy is different from conventional ROS probes, in which ROS has been utilized to "turn-on" fluorescence for imaging/detection (Table S1). Although those turn-on ROS probes are valuable and have been widely used for cell and peripheral target imaging (19–25, 27–34), they are limited to single-wavelength (single-color) imaging, by which it is difficult to differentiate the imaging signal before and after probe turning on, particularly for microscopic imaging. Our approach is to design imaging probes that can provide significant wavelength shift on ROS reaction (Fig. 1). At the microscopic level, the shifting could be used for dual-wavelength (dual-color) imaging on reacting with ROS. The benefits of dual-color imaging include providing more confident information, because the signal changes from both wavelengths/channels are interlocked, and the imaging information from one channel could be used to validate information from another channel. At the macrolevel of whole-brain NIRF imaging, the shifting could create a transformation from "visible (long emission)" to "invisible (short emission)" for a near-IR (NIR) camera/filter (640–900 nm) (Fig. 1), which could provide large signal margins between control and experimental groups.

Our probe design was inspired by the chemistry of glow sticks, in which oxalate ester reacts with H_2O_2 to generate chemiluminescence. When oxalate is mixed with H_2O_2, it converts into 1,2-dioxetanedione, which is not stable and instantly decomposes to generate CO_2 and release photons (35, 36). Nanoparticles containing oxalate and dyes have been used to detect H_2O_2 in vitro and in vivo via chemiluminescence (37–39). Our design strategy is different from chemiluminescent nanoparticles, which use oxalate as an exciting source for a fluorophore that is confined inside the nanoparticle. In our design, oxalate, which was used as a sensing moiety, was incorporated into the curcumin scaffold to produce probes with excitation (Ex) and emission (Em) in the NIR imaging window (640–900 nm) (Fig. 2*A*). After it reacted with ROS, the oxalate moiety was removed, and this removal consequentially led to dramatic blue shifts of Ex/Em wavelengths. These significant shifts can be used for dual-color microscopic imaging and can provide a visible to invisible transformation for macrolevel NIRF imaging of whole brains.

The additional important benefit of the oxalate ester moiety includes its contribution to longer Ex/Em, which is crucial for deep tissue light penetration in NIRF imaging. In our previous studies, we successfully extended the Ex/Em of curcumin via a pull–push system, in which BF_2 and *N*,*N*′-dimethylaminophenyl served as pull and push moiety, respectively (40). We reasoned that, on replacing BF_2 with oxalate boron ester, the Ex/Em wavelengths could be further elongated, because the electronic density of ester is more delocalized than that of fluorides. It is well-documented that a smaller HOMO and LUMO energy gap could lead to longer Ex/Em (41, 42), and a more electron delocalized oxalate ester could principally lead to a smaller HOMO/LUMO energy gap in CRANAD-61 than that in CRANAD-2.

Synthesis and Properties of CRANAD-61. The synthetic route for CRANAD-61 is shown in Fig. S1, and its structure was confirmed by ^{1}H NMR, ^{13}C NMR, and LC-MS (43–45). Computation data confirmed that the HOMO/LUMO gap of CRANAD-61 was smaller than that for CRANAD-2 (2.64 vs. 2.81 eV) (Fig. 2*B*). Its Ex peak is around 675 nm, and Em is around 760 nm in ethanol (Fig. 2*C*). As expected, CRANAD-61 does provide much longer Ex/Em than CRANAD-2 (Ex/Em 640/720 nm for CRANAD-2 vs. 675/760 nm for CRANAD-61). CRANAD-61 was fairly stable under physiological conditions. We found no significant fluorescence changes of CRANAD-61 in PBS buffers with pH 6.0, 6.7, 7.0, and 7.4 (Fig. S2 *A–D*). We performed in vitro ROS tests in 20% DMSO PBS (pH 7.4) buffers because of the better solubility and insignificant quenching (Fig. S2 *E* and *F*). Other in vitro tests were performed in 5% DMSO buffers.

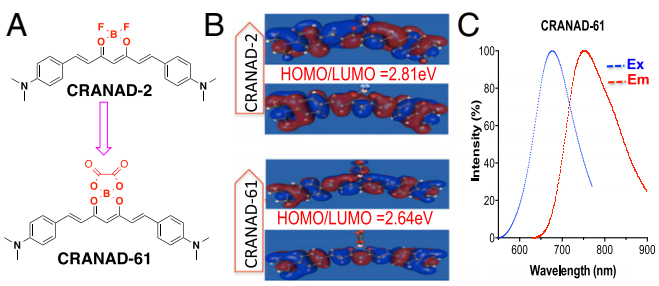

Fig. 2. (*A*) The structures of CRANAD-2 and CRANAD-61. (*B*) HOMO/LUMO of CRANAD-2 and CRANAD-61. The energy gap of CRANAD-61 is smaller than that of CRANAD-2. (*C*) Ex and Em spectra of CRANAD-61 in ethanol.

We found that its Em peak shifted to 810 nm in both 5 and 20% DMSO PBS buffers (Fig. S2*E*), and the probe formed larger particles in the 20% DMSO solution than that in the 5% DMSO solution (342 ± 27 vs. 186 ± 28 nm, $n = 4$) (Fig. S2*G*). The Em shifting could be primarily ascribed to J aggregation (46, 47) in the particles. We observed a slight fluorescence intensity decrease (5%) at 810 nm when 20% DMSO was used (Fig. S2*H*), which is likely caused by the oxidative capacity of DMSO (48). In addition, log *P* of CRANAD-61 was 2.24 in an octanol/water system, and quantum yield was 0.55% with indocyanine green (ICG) as the reference.

In Vitro Solution Testing with Various ROS. We first investigated whether CRANAD-61 was responsive to H_2O_2 and what the product of the reaction with H_2O_2 was. We incubated CRANAD-61 with 250 nM H_2O_2 and used liquid chromatography-mass spectrometry (LC-MS) to monitor the reaction. After 5 min, we observed a peak on LC-MS, which suggested the product was CRANAD-5 (Fig. S3*A*). After 30 min, CRANAD-61 completely disappeared, and the reaction mixture was subjected to a fluorescence spectral testing. We found that the Ex/Em spectra were consistent with CRANAD-5, further confirming that the reaction product was CRANAD-5 (Fig. S3*B*). To investigate the fluorescence response of CRANAD-61 in the presence of H_2O_2, 2.5 μM CRANAD-61 and 5.0 μM H_2O_2 were incubated in 20% DMSO PBS solution (pH 7.4). Fluorescence changes were monitored using dual-Em wavelengths of CRANAD-61 and CRANAD-5 (Ex/Em = 500/570 nm). We recorded the time course of the changes in fluorescence intensities at 570 and 810 nm. Indeed, we found that the reaction between H_2O_2 and CRANAD-61 was very fast. We observed an apparent increase in fluorescence intensity after a 1-min incubation at 570 nm. We also observed a fluorescence intensity decrease at 810 nm, indicating that CRANAD-61 was converted to CRANAD-5 (Fig. 3*A*). Remarkably, we found that CRANAD-61 was not only rapidly responsive to H_2O_2 but also, very sensitive to low concentrations of H_2O_2. At 5.0 nM H_2O_2, an apparent fluorescence intensity increase could be easily detected at 570 nm (Fig. S4*A*). The properties of CRANAD-61 for ROS detection seem to be different from most of the reported probes, which either are not sensitive enough for low concentrations of ROS or have slow responses.

Surprisingly, while investigating the specificity of CRANAD-61 for different ROS, we found that, other than H_2O_2, it was also very sensitive to other ROS, including $O_2^{\bullet-}$, $^{\bullet}OH$, OCl^-, TPHBP, and $NO^{\bullet}$ (Fig. 3*B* and Fig. S5). As no previous reports suggested that the oxalate moiety could be sensitive to other ROS, this was an unanticipated but beneficial finding. Among these ROS, CRANAD-61 showed the strongest responses for $O_2^{\bullet-}$ (Fig. 3*B*). Similar to the response to H_2O_2, CRANAD-61 also showed a fast and sensitive response to all of the tested ROS, which was concentration-dependent and reached a plateau at a 1:2 CRANAD-61:ROS ratio (Fig. 3*C* and Fig. S4 *B*–*E*). Interestingly, we also found that high ROS concentrations could lead to the decrease of intensities, which is likely caused by the photobleaching effect of ROS (49).

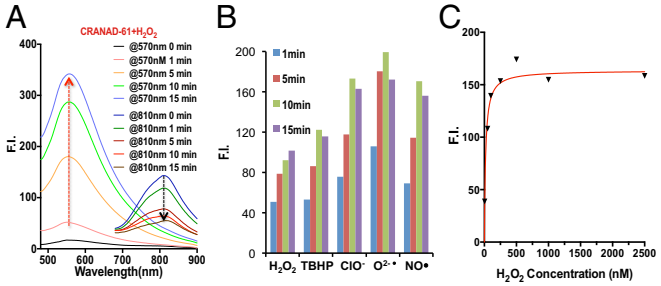

Fig. 3. In vitro testing of CRANAD-61 with various ROS. (*A*) Fluorescence intensity (F.I.) increases at 570 nm after CRANAD-61 incubation with ROS at different time points (Ex = 460 nm). (*B*) Spectral changes of CRANAD-61 after incubating with H_2O_2 at different time points. Note the increase in intensity at 570 nm and decrease in intensity at 810 nm (Ex = 675 nm). (*C*) Concentration-dependent intensity change of CRANAD-61 with ROS (H_2O_2 as a representative).

In Vitro Solution Fluorescence Spectral Testing of CRANAD-61 with Aβs. Our previous studies showed that curcumin analogs CRANAD-X (X = 2, 3, 5, and 58) could interact with Aβ species (40, 44, 50). Therefore, the next step was to investigate whether CRANAD-61 could interact with Aβs. To that end, we incubated CRANAD-61 with Aβs and found that CRANAD-61 was capable of binding to monomeric ($K_d = 3.2 \pm 1.5$ nM), oligomeric ($K_d = 3.8 \pm 1.1$ nM), and aggregated Aβs ($K_d = 38.1 \pm 14.7$ nM), with moderate fluorescence intensity increases (Fig. S6*A*). In Aβ plaques, metal ions always coexist with Aβ species (15). To investigate their possible quenching effects, we performed experiments with Cu(II), Fe(II), and Fe(III) in the presence of Aβ aggregates with or without H_2O_2. We found that metal ions could slightly quench the fluorescence of CRANAD-61 itself [5, 7, and 5%, respectively, for Cu(II), Fe(II), and Fe(III)] (Fig. S6*B*). However, in the presence of Aβ, the total intensity of CRANAD-61 was not significantly decreased, except for $CuSO_4$, with which an 11.4% decrease was observed (Fig. S6*C*). This quenching effect likely plays an insignificant role in the disappearance of the fluorescent signal in vivo, because we used much higher relatively concentrations of metal ions (Aβ/metal = 1) than those under real physiological conditions in vivo. Moreover, as we expected, the intensity was decreased when H_2O_2 was added because of the reaction of H_2O_2 and CRANAD-61 (Fig. S6 *D*–*F*). Histological staining of AD brain slices also showed that CRANAD-5 and CRANAD-61 could bind to Aβ plaques (Fig. S6 *G* and *H*).

Blood–Brain Barrier Testing of CRANAD-61. To investigate blood–brain barrier (BBB) penetration of CRANAD-61, we first conducted in vitro parallel artificial membrane permeability assay–BBB assay (51) and found the permeability (P_e) = 5.08×10^{-6} cm/s, suggesting that it has a strong potential for BBB penetration. In addition, we also injected BALB/c mice with CRANAD-61 using our previously reported protocol (40, 44). Fluorescence spectra from the brain homogenates suggested that CRANAD-61 penetrated the BBB (Fig. S7).

Two-Photon Microscopic Imaging of AD Mice for Identifying Active Plaques and CAAs. Aβ plaques and CAAs are distinct Aβ protein aggregates that appear in AD brains. Morphologically, Aβ plaques are roughly spherical structures with fibrous edges in the parenchyma, and CAAs are Aβ depositions on the outer surface of blood vessels as discontinuous ring-like shapes (10, 52, 53). Biochemically, Aβ aggregates/deposits contain distinct β-sheet structures that can be labeled by many amyloid binding dyes, including Thioflavin S, a dye that has been used as histologic gold standard for labeling Aβ deposits in tissue (54), and fluorostyrylbenzene (FSB), a widely used dye for Aβ plaque imaging (10, 53, 55). In this study, we used colocalization of FSB signal (blue in Fig. S8*A*) and CRANAD-61 signal (red in Fig. S8*A*) as the criterion for amyloid labeling (Fig. S8*A*). To quantify the fluorescence change of individual amyloid deposits, the outlines of plaques and CAAs were traced manually in the FSB *Z*-stack images.

To investigate whether it is feasible to identify active plaques and CAAs, we used dual-color two-photon imaging to examine the labeling properties of CRANAD-61 at the microlevel. We i.v. injected 14-mo-old APP/PS1 mice with CRANAD-61 followed by imaging at various time points. Our data showed that, 5 min after i.v. injection, CRANAD-61 crossed the BBB into brains and clearly labeled Aβ plaques and CAAs (Fig. 4 *A* and *C*). Primary fluorescence Em of CRANAD ranged initially from 640 to 680 nm (red in Fig. 4 *A* and *C*). Time-lapse imaging of the same regions showed that there was an obvious blue shift of the Em after 60 min. The signal from the 640- to 680-nm channel decreased, while the signal from the 500- to 550-nm channel (green in Fig. 4 *B* and *D*)

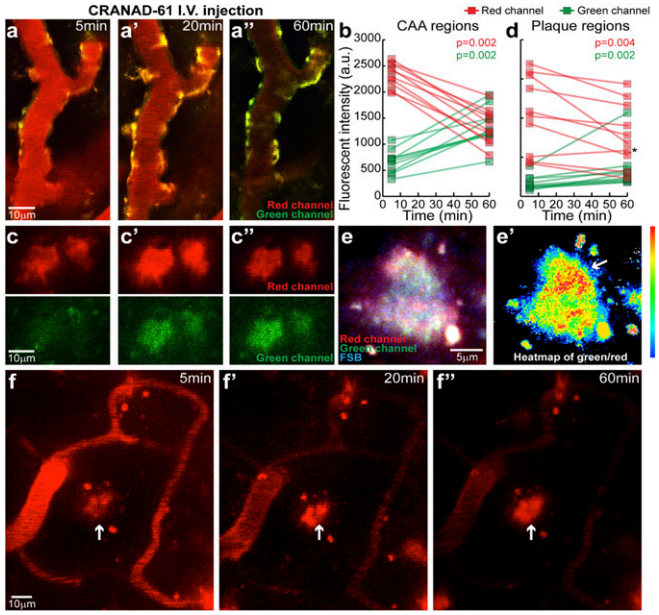

Fig. 4. In vivo dual-color two-photon imaging of CAA (*A*, *A′*, *A″*) and plaques (*C*, *C′*, *C″*) of APP/PS1 mice after i.v. injection of CRANAD-61 at different time points (5, 20, and 60 min), indicating that CRANAD-61 was able to cross BBB and specifically label plaques and CAAs. CRANAD-61 initially binds to amyloid with red fluorescence Em. Over the time of imaging, intensity in the red fluorescence channel decreased, while intensity in the green fluorescence channel increased, indicating ongoing conversion of CRANAD-61 into CRANAD-5 (*B* and *D*; n = 10 imaged amyloid deposits for each group; data shown as an individual point). Wilcoxon matched pairs signed rank tests were used for statistical testing between different time points. A $P < 0.05$ level was regarded as statistically significant. The asterisk indicates that one plaque showed no apparent conversion. a.u., arbitrary unit. (*E*) Example of an amyloid plaque colabeled with FSB and CRANAD-61 imaged in vivo at high magnification. The image was superimposed from acquisition at 800-nm Ex (FSB; blue channel) and 900-nm Ex (CRANAD-61; red and green channels). A heat map of the fluorescence intensity ratio between green and red channels (*E′*) indicated microregions in the plaque with a higher conversion rate (arrow). (*F*) Representative images of one plaque that showed no decrease in the red fluorescence intensity at 5, 20, or 60 min (arrows; *F*, *F′*, *F″*), while the free dye in the blood was significantly reduced.

clearly increased (Fig. 4 *B* and *D*). The appearance of green fluorescence over time was consistent with the expected conversion from CRANAD-61 to CRANAD-5, which is able to interact with various Aβs (43) (Fig. S6*H*). The interlocked changes from the red channel and from the green channel suggest the existence of a high ROS level around Aβ plaques and CAAs, which therefore, could be considered active plaques and active CAAs.

As expected, we also observed plaques in which the signal intensity did not substantially decrease in the red channel, and this echoed by insignificant intensity increase in the green channel during the 60-min imaging, suggesting that these plaques were surrounded by a low ROS level and therefore, could be considered inactive/silent (Fig. 4*F*). Notably, we found that the conversion rates in CAAs were more significant than those in the plaques obtained both from images and from quantification (Fig. 4 *B* and *D*), and this phenomenon provides evidence that CAA is a critical player in AD pathology (56).

Interestingly, the spectral shifting property of CRANAD-61 can be used as a ratiometric readout for local concentration of ROS around plaques for mapping the heterogeneity of a plaque. When imaged at a higher magnification, plaque microregions showed a differential rate of CRANAD-61 to CRANAD-5 conversion (Fig. 4*E*). A ratiometric measurement identified distinct microregions of the plaque that had a particularly high conversion rate, suggesting a high concentration of ROS at these locations. This result is consistent with previous reports of plaques with "hotspots," which contain concentrated Aβ42 and have a higher degree of toxicity to surrounding neurites (14).

In Vitro Phantom Imaging with NIRF Imaging Parameters. In principle, the wavelength-shifting property of CRANAD-61 could also be used for NIRF imaging of ROS at a macrolevel. The Ex and Em of CRANAD-61 ideally fit in the NIR imaging window (640–900 nm). On reacting with ROS, the oxalate moiety is removed, and this removal leads to a dramatic blue shift of Ex/Em wavelengths into a non-NIR window (<640 nm). The shift from an NIR window to a non-NIR window produced a transformation from "visible" to "invisible" for an NIR camera. With this transformation, the margin between control and experimental groups can be maximized. To investigate the feasibility of CRNAD-61's visible to invisible phenomenon for NIRF imaging, we performed in vitro imaging with the following parameters: Ex = 640 nm and Em = 740 nm. As expected, the CRANAD-61 signal gradually disappeared (became invisible) with the increase of ROS concentrations (Fig. S8*B*), indicating that it was feasible to capture the transformation from visible to invisible in the NIR imaging window. Remarkably, a similar transformation phenomenon was observed when CRANAD-61 was incubated with ROS in mouse brain homogenate, a mimic of biologically relevant environment (Fig. S8*C*).

Application of CRANAD-61 for NIRF Imaging of ROS in AD. To investigate whether CRANAD-61 can be used for imaging ROS in AD brains, we used an APP/PS1 mouse model, a widely used AD mouse model (57). We used a group of 12-mo-old mice to validate the existence of higher ROS concentrations in AD brains. (Note that the comparison only provides a relative level of ROS in AD brain and healthy control brains. Obviously, control brains should also have certain concentrations of ROS.) Images were captured at different time points after i.v. injection of CRANAD-61. We found that the NIRF signals in AD brains were significantly lower than those in the control group at 30, 60, 120, and 240 min after i.v. injection of CRANAD-61. Relative differences $[R_{(AD/WT)}]$ between AD brains and WT brains $[R_{(AD/WT)} = F_{(AD)}/F_{(WT)}]$ were 0.59-, 0.50-, 0.41-, and 0.29-fold at 30, 60, 120, and 240 min after probe injection, respectively (Fig. 5 *A* and *B*). Notably, the signal ratio $R_{(AD/WT)}$ was decreasing from 30 to 240 min (Fig. 5*C*), which is consistent with two-photon imaging results (the decrease in red channel). Although the decrease of CRANAD-61 signal was a combination of clearance and conversion to CRANAD-5, the slope in Fig. 5*C* was negative, suggesting that the disappearance rate of CRANAD-61 signal in AD brains was faster than that in WT brains, which could be ascribed to the higher ROS concentrations in AD brains. However, because of the fact that Ex/Em wavelengths of CRANAD-5 are too short for in vivo NIRF imaging, we were unable to report the change in $R_{(AD/WT)}$ with CRANAD-5 signal.

CRANAD-61 for Monitoring ROS-Level Changes in AD Mice of Different Ages. To investigate whether CRANAD-61 can be used for monitoring the ROS concentration changes at different ages in AD brains, we imaged 4- and 18-mo-old groups of APP/PS1 mice and age-matched control groups. Interestingly, at a young age of 4 mo old, the difference between APP/PS1 and control WT mice at early time points was negligible. Interestingly, at the early time points, the NIRF signal in the APP/PS1 group was slightly higher than that in the WT group, likely because of the fact that the fluorescence intensity of CRANAD-61 could be increased after its binds to Aβs (Fig. S6*A*). Apparent differences in 4-mo-old mice could be found at 60 and 120 min after the probe injection (Fig. S8*D*). In the 18-mo-old groups, significant differences could be observed at all of the time points. Importantly, an apparent time point difference for the maximal NIRF signals in AD and WT mice (10 vs. 30 min) could be observed (Fig. S9 *A* and *B*), suggesting the high ROS level in AD mice could lead to a faster and earlier signal loss. Interestingly, two-phase signal decay could

also be seen in the AD group (Fig. S9*B*). We found that there was a dramatic change in ROS levels from 4 [$R_{(WT/AD)} = 1.08$] to 12 mo [$R_{(WT/AD)} = 2.00$] (Fig. 5*D*), which is remarkable, and this may be related to the behavioral changes in APP/PS1 mice during this period of time. It is known that there are no behavioral differences between APP/PS1 mice and WT before 9 mo of age, while apparent abnormalities, including memory changes, in APP/PS1 mice could be observed after 9 mo of age (57). Moreover, Aβ loading in APP/PS1 mice increases rapidly from 6 to 10 mo of age. High concentrations of ROS may contribute to this cognitive change and Aβ increase. In addition, the change between 4- and 12-mo-old mice [$R_{(WT/AD)}$ from 1.08 to 2.00] was larger than the change between 12- and 18-mo-old mice [$R_{(WT/AD)}$ from 2.00 to 2.21] (Fig. 5*D*), most likely suggesting that ROS generation was reaching a plateau during the transition from 12 to 18 mo of age.

ROS Levels in the Blood of AD and Control WT Mice. We investigated whether the differences in NIRF signals between AD mice and WT mice are caused by the differences in ROS levels in blood. We found no significant differences between the blood samples from AD mice and WT mice (Fig. S9), suggesting that the difference in NIRF signals from brains could not be ascribed to ROS in the blood.

Discussion

It has been established that high concentrations of ROS are highly harmful for human health. However, there is no clear cutoff that defines the detrimental ROS concentration. In the past, several imaging probes for ROS have been reported and successfully applied for cell imaging and in vivo imaging. Nonetheless, none of them have been applied for in vivo brain imaging. In this report, we showed that CRANAD-61 was a fast responding and a highly sensitive probe for ROS that could be used for imaging ROS at micro- and macrolevels in brains of AD mice. In particular, our two-photon imaging data suggested that the local ROS concentrations in plaques could be measured with the ratiometric readout from the dual-imaging channels. Using dual-color two-photon imaging, it could be feasible to distinguish active and inactive/silence plaques and CAAs in vivo. Moreover, the ratiometric readout could also be used for mapping the heterogeneity of a plaque, showing that the microregions of high ROS level in a plaque are similar to hotspots reported previously (10, 14). Mounting evidence suggests that brain vascular dysfunction contributes substantially to AD pathology (56), and our observation of fast conversion rates of CRANAD-61 into CRANAD-5 around CAAs likely provides strong support for this speculation. Our method for identifying active and inactive/silent plaques could potentially be used to investigate the controversy surrounding the neurotoxicity of plaques and CAAs (1, 6, 7).

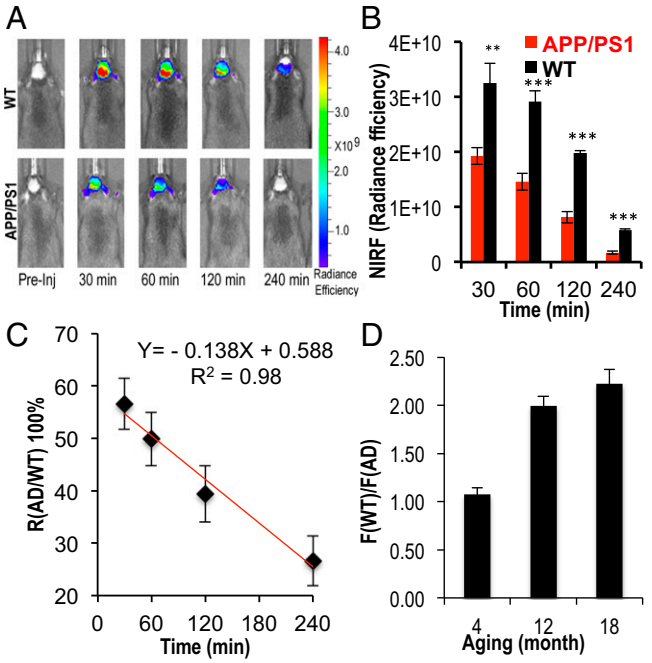

Fig. 5. In vivo NIRF imaging with CRANAD-61. (*A*) Representative images of WT and APP/PS1 mice after i.v. injection with CRANAD-61 at 30, 60, 120, and 240 min. (*B*) Quantification of images in *A*. Note that NIRF signals from WT are significantly higher than that from APP/PS1 mice. $^{**}P < 0.01$, $^{***}P < 0.005$. (*C*) Changes of the NIRF signal ratio $R_{(AD/WT)}$ [$R_{(AD/WT)} = F_{(AD)}/F_{(WT)}$] from 30 to 240 min. The negative slope suggested that the disappearance rate of the CRANAD-61 signal in AD brains was faster than in WT brains. (*D*) Changes of relative ROS levels in APP/PS1 mice of different ages. There was a dramatic increase of ROS levels from age 4 to 12 mo old.

At the macrolevel, we showed that CRANAD-61 could be used for detection of the differences in the total ROS levels in AD and WT brains and for monitoring of the increase of ROS with the progression of AD. Nonetheless, it is not clear how ROS concentrations change with the advancement of AD or in response to different treatments, such as combination therapy with anti-Aβ antibody, antioxidants, or antiinflammatory drugs. We believe that in vivo imaging using CRANAD-61 will provide answers to these daunting but fundamental questions at micro- and macrolevels and will potentially guide development of AD therapeutic strategies.

In this report, to design the probe for ROS sensing, we utilized the chemistry of glow sticks, in which oxalate ester reacts with H_2O_2 (35, 36). Surprisingly, we found that, in addition to H_2O_2, CRANAD-61 was also responsive for other ROS. In this report, we used curcumin scaffold to show the reactivity of oxalate ester with ROS. We believe that this oxalate ester-based strategy can also be integrated into other scaffolds, such as the cyanine dye family. In addition, we showed that, on installation of oxalate boron ester, the Ex/Em wavelengths could be further extended into NIR range because of smaller HOMO and LUMO energy gaps. Our oxalate-based ROS probe represents a unique category of ROS probe and is a platform for detecting ROS via both microscopic and NIRF imaging. We believe that this design strategy can be extended to other imaging probes as well. Therefore, this strategy can have a broad impact for designing imaging probes.

For imaging at the microlevel, the benefits of wavelength shifting are obvious, because it could be utilized for dual-color imaging, which can provide more reliable information than single-color imaging. With the capacity of dual-color two-photon imaging, we can reliably differentiate active and silent plaques and CAAs, because the signal changes from each channel are reciprocally coupled. For macrolevel NIRF imaging, the wavelength shifting could be considered a transformation from visible to invisible for an NIR camera or filter, and this "turn-off" can provide a significant signal difference between the experimental and control groups. Conventional molecular imaging requires that the target-bound probe and free probe have significantly different retention times to achieve contrast. However, in the absence of target binding, as in the case with ROS, the differences in retention times cannot be measured. Nonetheless, the transformation of CRANAD-61 on ROS reaction could be used to measure the difference. The drawback of CRANAD-61's wavelength shifting at macrolevel NIRF is a lost-of-signal contrast. However, this drawback could be overcome by designing probes that have Ems in the NIR window both before and after ROS reaction.

Clearly, ROS concentrations in a living being cannot be measured in absolute values because of their highly reactive property and short lifetime. It is also difficult to validate in vivo data with ex vivo measurement, since the killing procedure generates abundant ROS. However, it is reasonable to provide relative measurements compared with healthy controls in vivo. Considering the complexity of living beings, other metabolic

processes, other than ROS, may have effects on the differences between AD and WT mice.

In summary, our results showed that CRANAD-61 was a highly sensitive, fast response, and BBB-permeable ROS imaging probe. Our imaging at both micro- and macrolevels could provide a more comprehensive picture of ROS in brains, which could lead to better understanding AD pathology and a better approach for AD drug discovery.

Materials and Methods

Materials, methods, and chemical synthesis are described in *SI Materials and Methods*. All animal experiments were approved by the Institutional Animal Use and Care Committee at Massachusetts General Hospital.

ACKNOWLEDGMENTS. We thank Pamela Pantazopoulos for proofreading this manuscript. This work was supported by NIH Grants K25AG036760 (to C.R.), R21AG050158 (to C.R.), and R03AG050038 (to C.R.).

1. Selkoe DJ (2011) Resolving controversies on the path to Alzheimer's therapeutics. *Nat Med* 17:1060–1065.
2. Jonsson T, et al. (2012) A mutation in APP protects against Alzheimer's disease and age-related cognitive decline. *Nature* 488:96–99.
3. Perry G, Cash AD, Smith MA (2002) Alzheimer disease and oxidative stress. *J Biomed Biotechnol* 2:120–123.
4. Markesbery WR (1997) Oxidative stress hypothesis in Alzheimer's disease. *Free Radic Biol Med* 23:134–147.
5. Maulucci G, et al. (2016) Imaging reactive oxygen species-induced modifications in living systems. *Antioxid Redox Signaling* 24:939–958.
6. Abbott A (2008) Neuroscience: The plaque plan. *Nature* 456:161–164.
7. Hefendehl JK, et al. (2016) Mapping synaptic glutamate transporter dysfunction in vivo to regions surrounding Aβ plaques by iGluSnFR two-photon imaging. *Nat Commun* 7:13441.
8. McLean CA, et al. (1999) Soluble pool of Abeta amyloid as a determinant of severity of neurodegeneration in Alzheimer's disease. *Ann Neurol* 46:860–866.
9. Lue LF, et al. (1999) Soluble amyloid beta peptide concentration as a predictor of synaptic change in Alzheimer's disease. *Am J Pathol* 155:853–862.
10. Condello C, Schain A, Grutzendler J (2011) Multicolor time-stamp reveals the dynamics and toxicity of amyloid deposition. *Sci Rep* 1:19.
11. Meyer-Luehmann M, et al. (2008) Rapid appearance and local toxicity of amyloid-beta plaques in a mouse model of Alzheimer's disease. *Nature* 451:720–724.
12. Spires TL, et al. (2005) Dendritic spine abnormalities in amyloid precursor protein transgenic mice demonstrated by gene transfer and intravital multiphoton microscopy. *J Neurosci* 25:7278–7287.
13. Xie H, et al. (2013) Rapid cell death is preceded by amyloid plaque-mediated oxidative stress. *Proc Natl Acad Sci USA* 110:7904–7909.
14. Condello C, Yuan P, Schain A, Grutzendler J (2015) Microglia constitute a barrier that prevents neurotoxic protofibrillar Aβ42 hotspots around plaques. *Nat Commun* 6:6176.
15. Bush AI, Tanzi RE (2008) Therapeutics for Alzheimer's disease based on the metal hypothesis. *Neurotherapeutics* 5:421–432.
16. Huang Y, Erdmann N, Peng H, Zhao Y, Zheng J (2005) The role of TNF related apoptosis-inducing ligand in neurodegenerative diseases. *Cell Mol Immunol* 2:113–122.
17. Wilkinson BL, Landreth GE (2006) The microglial NADPH oxidase complex as a source of oxidative stress in Alzheimer's disease. *J Neuroinflammation* 3:30.
18. Bolmont T, et al. (2008) Dynamics of the microglial/amyloid interaction indicate a role in plaque maintenance. *J Neurosci* 28:4283–4292.
19. Pu K, et al. (2014) Semiconducting polymer nanoparticles as photoacoustic molecular imaging probes in living mice. *Nat Nanotechnol* 9:233–239.
20. Guo H, Aleyasin H, Dickinson BC, Haskew-Layton RE, Ratan RR (2014) Recent advances in hydrogen peroxide imaging for biological applications. *Cell Biosci* 4:64.
21. Dickinson BC, Chang CJ (2008) A targetable fluorescent probe for imaging hydrogen peroxide in the mitochondria of living cells. *J Am Chem Soc* 130:9638–9639.
22. Dickinson BC, Srikun D, Chang CJ (2010) Mitochondrial-targeted fluorescent probes for reactive oxygen species. *Curr Opin Chem Biol* 14:50–56.
23. Abo M, et al. (2011) Development of a highly sensitive fluorescence probe for hydrogen peroxide. *J Am Chem Soc* 133:10629–10637.
24. Koide Y, Urano Y, Kenmoku S, Kojima H, Nagano T (2007) Design and synthesis of fluorescent probes for selective detection of highly reactive oxygen species in mitochondria of living cells. *J Am Chem Soc* 129:10324–10325.
25. Karton-Lifshin N, et al. (2011) A unique paradigm for a Turn-ON near-infrared cyanine-based probe: Noninvasive intravital optical imaging of hydrogen peroxide. *J Am Chem Soc* 133:10960–10965.
26. Chen ZJ, Ren W, Wright QE, Ai HW (2013) Genetically encoded fluorescent probe for the selective detection of peroxynitrite. *J Am Chem Soc* 135:14940–14943.
27. Robinson KM, et al. (2006) Selective fluorescent imaging of superoxide in vivo using ethidium-based probes. *Proc Natl Acad Sci USA* 103:15038–15043.
28. Koide Y, Urano Y, Hanaoka K, Terai T, Nagano T (2011) Development of an Si-rhodamine-based far-red to near-infrared fluorescence probe selective for hypochlorous acid and its applications for biological imaging. *J Am Chem Soc* 133:5680–5682.
29. Xu Q, et al. (2015) Development of imidazoline-2-thiones based two-photon fluorescence probes for imaging hypochlorite generation in a co-culture system. *Angew Chem Int Ed Engl* 54:4890–4894.
30. Yu F, et al. (2011) A near-IR reversible fluorescent probe modulated by selenium for monitoring peroxynitrite and imaging in living cells. *J Am Chem Soc* 133:11030–11033.
31. Yu H, Xiao Y, Jin L (2012) A lysosome-targetable and two-photon fluorescent probe for monitoring endogenous and exogenous nitric oxide in living cells. *J Am Chem Soc* 134:17486–17489.
32. Zhang Q, et al. (2012) A three-channel fluorescent probe that distinguishes peroxynitrite from hypochlorite. *J Am Chem Soc* 134:18479–18482.
33. Rosenthal J, Lippard SJ (2010) Direct detection of nitroxyl in aqueous solution using a tripodal copper(II) BODIPY complex. *J Am Chem Soc* 132:5536–5537.
34. Kundu K, et al. (2009) Hydrocyanines: A class of fluorescent sensors that can image reactive oxygen species in cell culture, tissue, and in vivo. *Angew Chem Int Ed Engl* 48:299–303.
35. Orosz G (1989) The role of diaryl oxalates in peroxioxalate chemiluminescence. *Tetrahedron* 45:3493–3506.
36. Chokshi HP, et al. (1990) Oxalate/hydrogen peroxide chemiluminescence reaction. A 19F NMR probe of the reaction mechanism. *Biomed Chromatogr* 4:96–99.
37. Shuhendler AJ, Pu K, Cui L, Uetrecht JP, Rao J (2014) Real-time imaging of oxidative and nitrosative stress in the liver of live animals for drug-toxicity testing. *Nat Biotechnol* 32:373–380.
38. Lee D, et al. (2007) In vivo imaging of hydrogen peroxide with chemiluminescent nanoparticles. *Nat Mater* 6:765–769.
39. Lee I-J, Hwang O, Yoo D-H, Khang G-S, Lee D-W (2011) Detection of hydrogen peroxide in vitro and in vivo using peroxalate chemiluminescent micelles. *Bull Korean Chem Soc* 32:2187–2192.
40. Ran C, et al. (2009) Design, synthesis, and testing of difluoroboron-derivatized curcumins as near-infrared probes for in vivo detection of amyloid-beta deposits. *J Am Chem Soc* 131:15257–15261.
41. Lakowicz J (1999) *Principles of Fluorescence Spectroscopy* (Plenum, New York), 2nd Ed.
42. Li E, Kim A, Zhang L (2007) Modeling excited states of fluorescent compounds with UV-Vis spectra calculations. *J Student Comp Chem* 1:1–72.
43. Ran C, Zhao W, Moir RD, Moore A (2011) Non-conjugated small molecule FRET for differentiating monomers from higher molecular weight amyloid beta species. *PLoS One* 6:e19362.
44. Zhang X, et al. (2013) Design and synthesis of curcumin analogues for in vivo fluorescence imaging and inhibiting copper-induced cross-linking of amyloid beta species in Alzheimer's disease. *J Am Chem Soc* 135:16397–16409.
45. Zhao Z, Hartmann H (2000) Synthesis of reactive condensation products of acetylacetone and their transformation into deeply coloured methine dyes. *J Prakt Chem* 342:249–255.
46. Deng Y, Yuan W, Jia Z, Liu G (2014) H- and J-aggregation of fluorene-based chromophores. *J Phys Chem B* 118:14536–14545.
47. Eisfeld A, Briggs JS (2006) The J- and H-bands of organic dye aggregates. *Chem Phys* 324:376–384.
48. Sweat FW, Epstein WW (1967) Dimethyl sulfoxide oxidations. *J Org Chem* 32:835–838.
49. Zheng Q, Jockusch S, Zhou Z, Blanchard SC (2014) The contribution of reactive oxygen species to the photobleaching of organic fluorophores. *Photochem Photobiol* 90:448–454.
50. Zhang X, et al. (2015) Near-infrared fluorescence molecular imaging of amyloid beta species and monitoring therapy in animal models of Alzheimer's disease. *Proc Natl Acad Sci USA* 112:9734–9739.
51. Wohnsland F, Faller B (2001) High-throughput permeability pH profile and high-throughput alkane/water log P with artificial membranes. *J Med Chem* 44:923–930.
52. Zhang X, et al. (2014) A bifunctional curcumin analogue for two-photon imaging and inhibiting crosslinking of amyloid beta in Alzheimer's disease. *Chem Commun (Camb)* 50:11550–11553.
53. Yuan P, et al. (2016) TREM2 haplodeficiency in mice and humans impairs the microglia barrier function leading to decreased amyloid compaction and severe axonal dystrophy. *Neuron* 90:724–739.
54. Bussière T, et al. (2004) Morphological characterization of thioflavin-S-positive amyloid plaques in transgenic Alzheimer mice and effect of passive Abeta immunotherapy on their clearance. *Am J Pathol* 165:987–995.
55. Sato K, Higuchi M, Iwata N, Saido TC, Sasamoto K (2004) Fluoro-substituted and 13C-labeled styrylbenzene derivatives for detecting brain amyloid plaques. *Eur J Med Chem* 39:573–578.
56. O'Brien JT, Thomas A (2015) Vascular dementia. *Lancet* 386:1698–1706.
57. Borchelt DR, et al. (1996) Familial Alzheimer's disease-linked presenilin 1 variants elevate Abeta1-42/1-40 ratio in vitro and in vivo. *Neuron* 17:1005–1013.